MACGHYVER

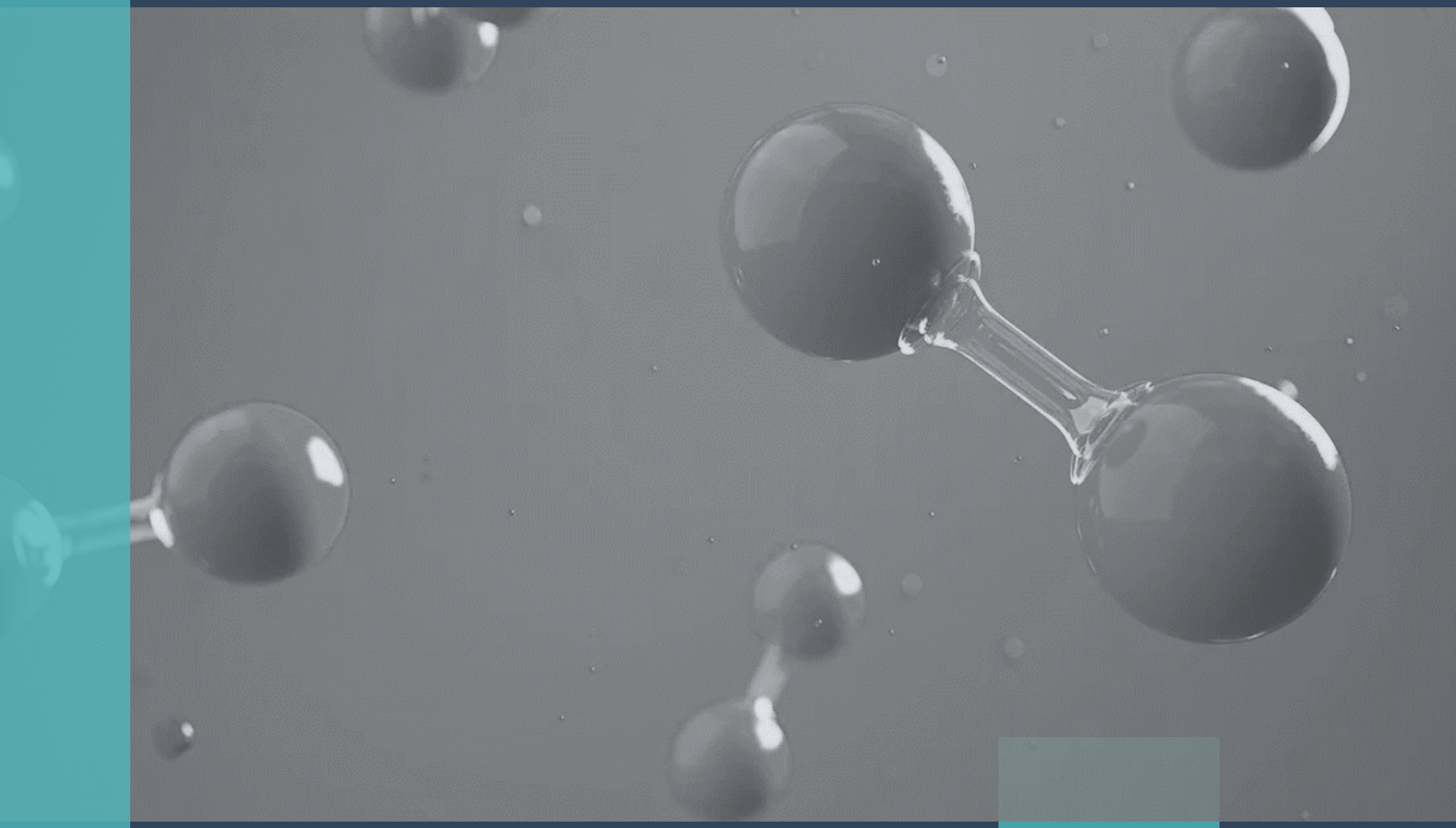

2023-08-30

D 2.1

PRIORITY LIST OF NON-CRM ELECTRODES

WP2 Non-CRM electrodes

This project has received funding from the European Innovation Council (EIC) under grant agreement No 101069981. The EIC receives support from the European Union's Horizon Europe Research and Innovation Program

Project	**Microfluidic Wastewater Treatment and Creation of Green Hydrogen Via Electrochemical Reactions (MACGHYVER)**
Grant number	101069981
Author(s)/Organisation(s)	Aleksandra Gladkova, Lydia Weseler, Maik Becker, Thomas Turek (TUC)
Work Package	WP2 Non-CRM electrodes
Delivery Date (DoA)	31.08.2023
Actual Delivery Date	31.08.2023
Abstract:	Current Deliverable 2.1 provides a priority list of non-CRM (non-precious metal materials) electrode materials for use in the microfluidic electrolyzer. The benchmark material overview of commercially available Ni-, Fe-based materials like foils, meshes (with applied nano/microparticles; gold plated), felts, and foams are presented. Evaluation of vital geometrical parameters (pore/mesh size, thickness of the samples) and physical properties (electrical characteristics, porosity, permeability, conductivity, and permeability) were evaluated. Optical electron microscope observations were used to examine the pore size. The electrochemical performance of electrodes (anodic and cathodic behaviour) in aqueous alkaline electrolytes containing potassium hydroxide (concentration range up to 32 wt.%) is investigated. As a result of this investigation, the most promising non-CRM electrodes for OER (steel felt and mesh) and HER (nickel mesh) have been selected for integration into a lab-scale experimental setup.

Document Revision History			
Date	**Version**	**Author/Contributor/ Reviewer**	**Summary of main changes**
15.08.2023	0.1	Aleksandra Gladkova, Lydia Weseler (TUC)	Draft V.1.
22.08.2023	0.2	Aleksandra Gladkova, Maik Becker, Lydia Weseler, Thomas Turek (TUC)	Draft V.2. Review and editing
24.08.2023	0.3	Abhilash Venkateshaiah & Wei Zhao (EDEN)	Quality control
30.08.2023	0.4	Aleksandra Gladkova, Maik Becker, Thomas Turek (TUC)	Final check

Dissemination Level		
PU	Public	☑
CO	Confidential, only for members of the consortium (including the EC)	□
PP	Restricted to other programme participants (including the EC Services)	□
RE	Restricted to a group specified by the consortium (including the EC Services)	□

MACGHYVER Consortium			
Participant Number	**Participant organisation name**	**Short name**	**Country**
1	Eden Tech	EDEN	France
2	Universidad De Castilla - La Mancha	UCLM	Spain
3	Technische Universiteit Delft	DELFT	Netherlands
4	Gottfried Wilhelm Leibniz Universitaet Hannover	LUH	Germany
5	Technische Universitat Clausthal	TUC	Germany
6	Politechnika Poznanska	POZ	Poland

CONTENTS

1. INTRODUCTION

The costs associated with cell and stack production are approximately 20% to 30% of the overall expenses of an alkaline electrolyzer. The use of non- critical raw materials (CRM) metals such as pure nickel, iron and its alloys with low cost compared to noble metals, such as platinum, and at the same time with sufficiently high electrocatalytic activity and corrosion resistance in an alkaline environment, are highly promising for alkaline water electrolysis (AWE) applications and can significantly reduce the cost of the final stack construction [1-3]. Geometry and physical parameters play an essential role in applying porous electrodes percolated by forced electrolyte flow [4]. An optimal combination of geometrical and physical properties can afford large contact areas, resulting in higher electrochemical performance (efficiency) and promoting correct flow regime conditions. On the one hand, the expanded surface area can enhance the charge transfer and, under certain circumstances, minimize gas crossing-over lowering the blocking between the active substrate and electrolyte. On the other hand, it can cause problems in homogeneous flow distributions preventing the reduction of interelectrode gaps and the electrode area to be increased via enlarged active 'material/electrolyte' interfaces and, in this case, electrodes with much smaller pore sizes and hydraulic permeability should be used.

Thus, it is important to reveal electrodes with optimal relatively large pore/mesh sizes, minimizing the pressure drop over them and which still maintain a sufficiently high surface area.

The following basic requirements for the microfluidic electrolyzer electrodes were made in order to find appropriate materials for further experimental evaluation:

1. non-CRM metals should be used;
2. thickness of the material should not exceed 1 mm;
3. metallic materials should possess a low specific electrical resistivity in order to be able to conduct electrical currents efficiently;
4. materials should have high structural surface area and branched surface morphology.

Based on the requirements, the primary goal of Deliverable 2.1 was to determine the optimal structure parameters of the industrially available non-CRM metals. The aim was to identify the most promising electrode materials that facilitate efficient hydrogen evolution reaction (HER) at the cathode (-) and oxygen evolution reaction (OER) at the anode (+) under optimal conditions of flow regime.

In order to achieve the goal, a comprehensive investigation was conducted on different types of 23 Ni- and Fe-based materials, such as foil, expanded and woven meshes, felts, and foams with various structural characteristics and geometrical and physical parameters. The impact of these parameters on the electrochemical performance of the materials was thoroughly studied.

2. SELECTION OF NON-PRECIOUS METAL ELECTRODES

Electrode materials commonly used in AWE are *nickel* and *stainless steel* due to their elevated intrinsic activity. Currently, most AWE adopts the electrodes as expanded and woven meshes, foam, and perforated plates or foil [5].

Each type of material has a set of advantages:

1) Metal mesh:

- high strength,
- being able to easily manufacture a desired shape or threads interlaced at right angles,
- high permeability,
- low cost compared to electrodes made from other techniques.

2) Metal foam:

- increased active surface area due to its porous structure,
- excellent three-dimensional network porous structure,
- average cost level,
- high permeability,
- the technique can be extended to produce a wide variety of electrodes.

3) Metal fibre felt:

- excellent three-dimensional network porous structure,
- high porosity,
- large specific surface area,
- uniform pore size distribution,
- high permeability,
- long-term stability.

Other promising material types described in the literature, due to their branched complex-structured surfaces or promising morphology for bubble removal, such as Incofoam (CVD, PVD technology) [6], lattice-structured materials (additive manufacturing) [7], powder

metallurgy, or electrodeposition [8], freeze casting materials [9], cluster-like nickel nanowire [10], phase inversion tape casting materials [11], have also been critically reviewed. However, materials produced by these methods are not represented at this stage of research in this deliverable due to the high cost of manufacturing or not applicable by the industrial sector because of non-reproducible unstable manufacturing processes.

In this work, 23 types of the industrially available Ni-, Fe-based materials (8 nickel meshes, 3 gold-plated meshes, 5 steel mashes, 4 nickel foams, 1 steel felt, 1 nickel felt, and 1 nickel foil) are characterized. Samples names, where in '*Ni mesh 250*' "Ni" is alloy, "mesh"- type of material, "250" - thickness of sample in μm; description of composition and supplier summarized in Tab. 1.

Table 1: Samples description and elemental composition of alloys used in the work. All materials are highlighted in various background colour with respect to figures.

№	Name	Supplier	Comment	Price, €
Foil				
1	Ni foil 61	Metall Jobst	Ni 2.4068 (Pure Ni 99,2 wt. %)	80-120
Mesh				
2	Ni mesh 250	Haver&Boecker OHG	Pure Ni 99 wt. %	
8	Ni mesh 127		Pure Ni 99 wt. %	
9	Ni mesh 384		Ni 2.4602+NiFe-GDE* (Hastelloy 2.4602, NiCr21Mo14W)	
15	Ni mesh 494		Ni 2.4819 (Hastelloy 2.4819, Ni-Mo-Cr-15W)	110-130
17	Ni mesh 157		Pure Ni 99 wt. %	
18	Ni mesh 700		Ni 2.4816 (Inconel 2.4816, NiCr15Fe8)	
19	Ni mesh 606		Ni 2.4602 (Hastelloy 2.4602, NiCr21Mo14W)	
23	Ni mesh 310	Dorstener Drahtwerke H. W. Brune&Co. GmbH	Ni 2.4060 (Pure Ni 99.6 wt. %)	120-300
11	Ni mesh gold-plated 165	Covestro AG. Dresdner silver and metal finishing GmbH (galvanic gilding)	Ni 99.2+ electroplated gold plating** (Pure Ni 99.2 wt. %)	1500-2000
14	Ni mesh gold-plated 221			
16	Ni mesh gold-plated 106			
10	St mesh 50	GKD-gebr. Kufferath AG	Stainless steel 1.4404 (AISI 316L, austenitic chromium-nickel-molybdenum stainless steel)	70-150
12	St mesh 406	Haver&Boecker OHG		40-150
13	St mesh 359		Stainless steel 1.4571 (AISI 316 Ti, austenitic chromium-nickel-stainless steel)	

Table 1: (continued)

21	St mesh 665	Sorst Streckmetall GmbH	Stainless steel 1.4404 (AISI 316L, austenitic chromium-nickel-molybdenum stainless steel)	
22	St mesh 1033			
Foam				
3	Ni foam 2500	Alantum Europe GmbH	Ni 99.9 (Pure Ni 99.9 wt. %)	1500-2000
4	Ni foam 1900			
5	Ni foam 310			
6	Ni foam 1400			
Felt				
7	St felt 130	BinNova GmbH&Co KG	Stainless Steel 1.4404 (AISI 316L, austenitic chromium-nickel-molybdenum)	1050
20	Ni felt 264			1200

*To produce the GDE, a suspension consisting of Ni particles, PTFE, iron lactate, iron gluconate and methyl cellulose is mixed. The suspension contains 4% by weight of methyl cellulose. After the GDE has been sprayed, it is sintered and the methyl cellulose is burned, so that the pores become free. After sintering, the GDE consists of (wt. %): 91.09 Ni particles (3-7 µm), 2.9% Fe (iron lactate and iron gluconate), 6 PTFE.
**Golden coating has very good electrical conductivity, is virtually corrosion-free and is therefore used in technical applications.

3. CHARACTERIZATION OF AVAILABLE MATERIALS

Photographs and light microscopic images of industrial available materials were taken with 4K high-resolution digital microscope VHX-7000 (Keyence, Belgium) (see Fig. 1) at magnifications ×100, ×200, ×300, ×700. By observation, Ni meshes have typical silvery or golden metallic, smooth cross-linked structures, while Ni foams show interconnected 3D channels and branched porous architecture.

Figure 1: 4k high-resolution digital microscope Modelreihe VHX-7000 (Keyence, Belgium)

The images of the electrode samples can be seen in Fig. 2 in multiple magnifications (due to the number of images shown on multiple pages).

(a)

(b)

sample ‘1 Ni foil 61’

Figure 2: (continued)

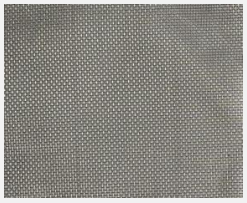

(a)

(b)
sample ‘2 Ni mesh 250’

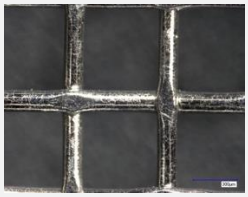

(c)

(a)

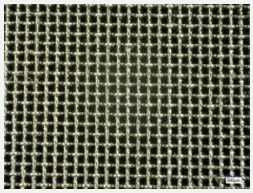

(b)
sample ‘8 Ni mesh 127’

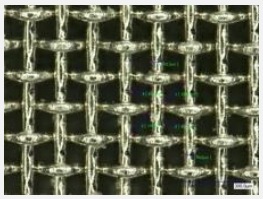

(c)

(a)

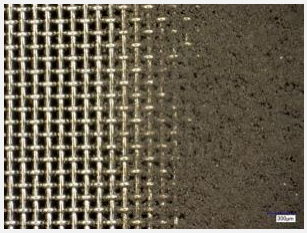

(b)
sample ‘9 Ni mesh 384’

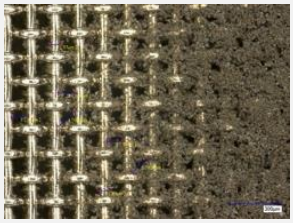

(c)

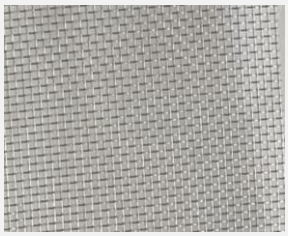

(a)

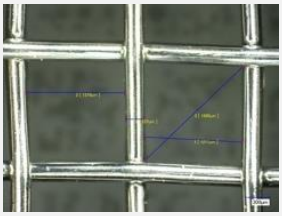

(b)
sample ‘15 Ni mesh 494’

(a)

(b)
sample ‘17 Ni mesh 157’

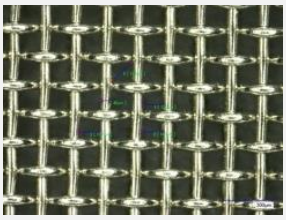

(c)

Figure 2: (continued)

(a)

(b)
sample ‘18 Ni mesh 700’

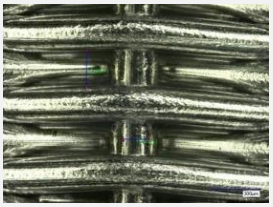

(c)

(a)

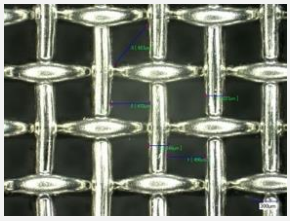

(b)
sample ‘19 Ni mesh 606’

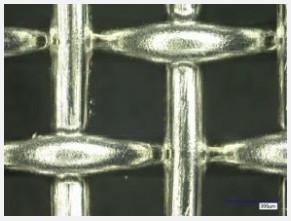

(c)

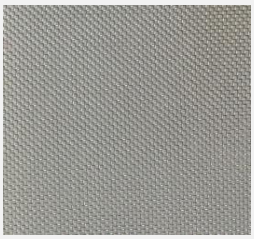

(a)

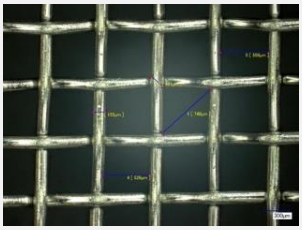

(b)
sample ‘Ni mesh 310’

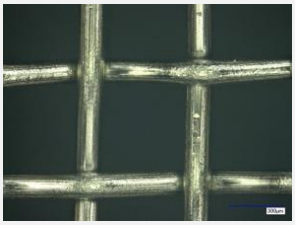

(c)

(a)

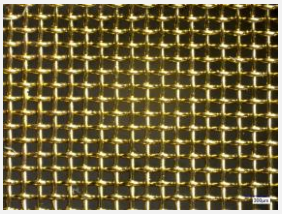

(b)
sample ‘11 Ni mesh gold-plated 165’

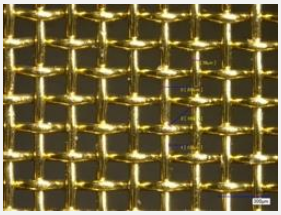

(c)

(a)

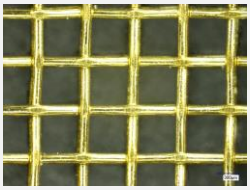

(b)
sample ‘14 Ni mesh gold-plated 221’

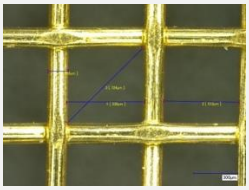

(c)

Figure 2: (continued)

(a)

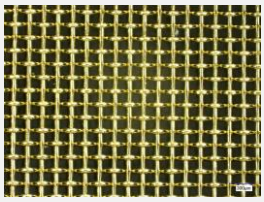

(b)

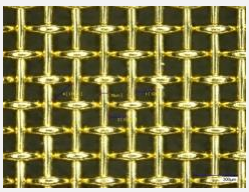

(c)

sample '16 Ni mesh gold-plated 106'

(a)

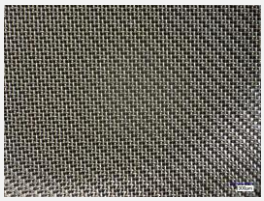

(b)

(c)

sample '10 St mesh 50'

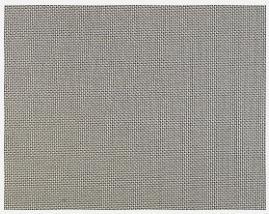

(a)

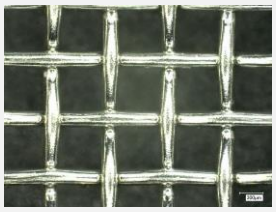

(b)

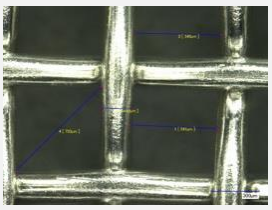

(c)

sample '12 St mesh 406'

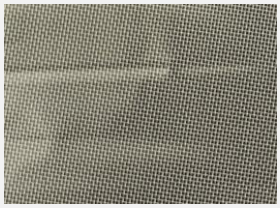

(a)

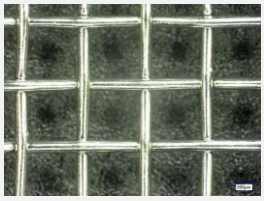

(b)

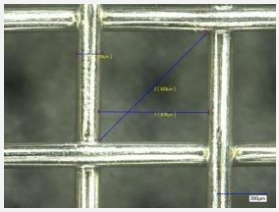

(c)

sample '13 St mesh 359'

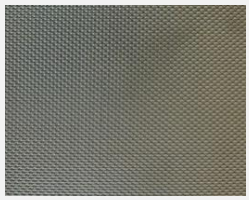

(a)

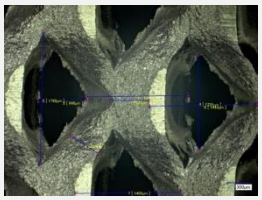

(b)

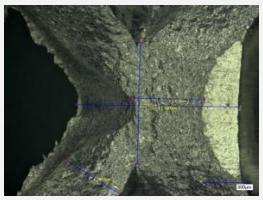

(c)

sample '21 St mesh 665'

(a)

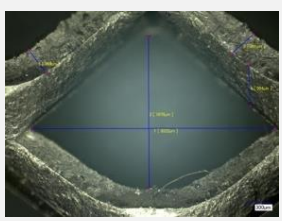

(b)

sample '22 St mesh 1033'

Figure 2: (continued)

(a)

(b)
sample ‘3 Ni foam 2500’

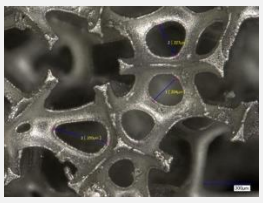

(c)

(a)

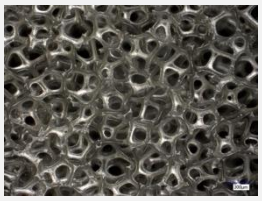

(b)
sample ‘4 Ni foam 1900’

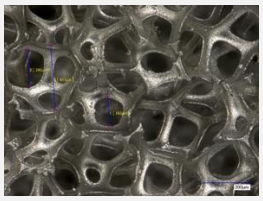

(c)

(a)

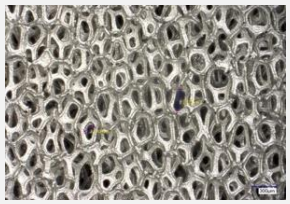

(b)
sample ‘6 Ni foam 1400’

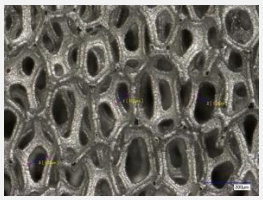

(c)

(a)

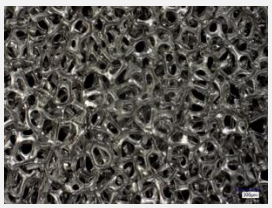

(b)
sample ‘5 Ni foam 310’

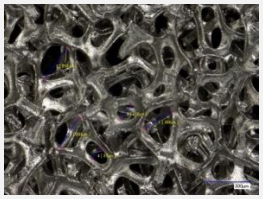

(c)

(a)

(b)
sample ‘7 St felt 130’

(c)

Figure 2: (continued)

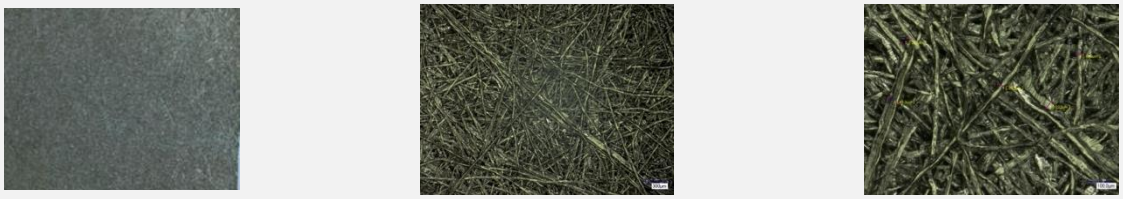

(a) (b) (c)

sample '20 Ni felt 264'

Figure 2: Photographs (a) and optical microscopic image of industrially available materials at magnifications ×100 (b) and ×200 (c)

4. GEOMETRICAL AND PHYSICAL PARAMETERS

Main geometrical and physical parameters measured during this work are presented comprehensively in Tab. 2.

Table 2: Main geometrical and physical parameters of commercially available materials studied in this work.

Number	Sample	Thickness of sample, *e th*/ µm	Diameter of stand (wire diameter), µm	Pore/ mesh size (width), *w*/ µm	Volumetric porosity, *ε*	Permeability, $k \cdot 10^{-13}$/ m^2	Specific electrical resistance, $\rho_v \cdot 10^{-3}$/ Ω cm	Density, ρ/ g·cm^{-3}
2	Ni mesh 250	250	100	500	0.793	9.14	2.62	8.81
8	Ni mesh 127	127	45	80	0.666	4.64	3.83	8.76
9	Ni mesh 384	384	60	80	0.581	1.52	3.46	8.90
15	Ni mesh 494	494	250	1120	0.849	15.40	51.1	8.47
17	Ni mesh 157	157	63	106	0.768	4.86	4.01	8.55
18	Ni mesh 700	700	120	120	0.679	21.60	21.1	8.32
19	Ni mesh 606	606	250	500	0.741	18.60	14.6	8.51
23	Ni mesh 310	310	150	485	0.819	-	4.12	8.90
11	Ni mesh gold-plated 165	165	60	128	0.751	5.97	3.86	8.63
14	Ni mesh gold-plated 221	221	140	500	0.788	6.75	2.66	8.67
16	Ni mesh gold-plated 106	154	63	106	0.763	4.77	3.61	8.65
10	St mesh 50	50	25	25	0.557	1.79	40.7	7.67
12	St mesh 406	406	200	500	0.768	12.70	316	7.61
13	St mesh 359	359	460	630	0.86	11.30	196	7.54

Table 3: (continued)

21	St mesh 665	665	433	1443	0.539	19.50	3.97	7.89
22	St mesh 1033	1033	360	2500	0.879	37.30	5.33	8.00
3	Ni foam 2500	2500	80	250	0.756	89.30	4.02	8.60
4	Ni foam 1900	1900	40	580	0.97	68.50	4.43	8.65
5	Ni foam 310	310	39	100	0.831	11.50	4.39	8.47
6	Ni foam 1400	1400	37	270	0.869	49.90	0.891	8.86
7	St felt 130	130	2	25	0.883	4.64	78.2	7.76
20	Ni felt 264	264	33	50	0.569	0.70	2.13	8.99
1	Ni foil 61	61	-	-	0.03	-	1.86	8.60

4.1. GEOMETRICAL PARAMETERS

4.1.1. THICKNESS OF ELECTRODE MATERIALS

The thickness of samples was evaluated by digital thickness dial gauge FD 50 (Käfer GmbH, Germany) (see Fig. 3).

Figure 3: Digital thickness dial gauge FD 50

Thicknesses of Ni meshes vary from 127 to 700 µm, Ni gold-plated meshes – from 106 to 221 µm, steel meshes – from 50 to 1033 µm, Ni foams – from 310 to 2500, steel felt – 130 µm, Ni felt – 264 µm, Ni foil – 61 µm (see Fig. 4, Tab. 2).

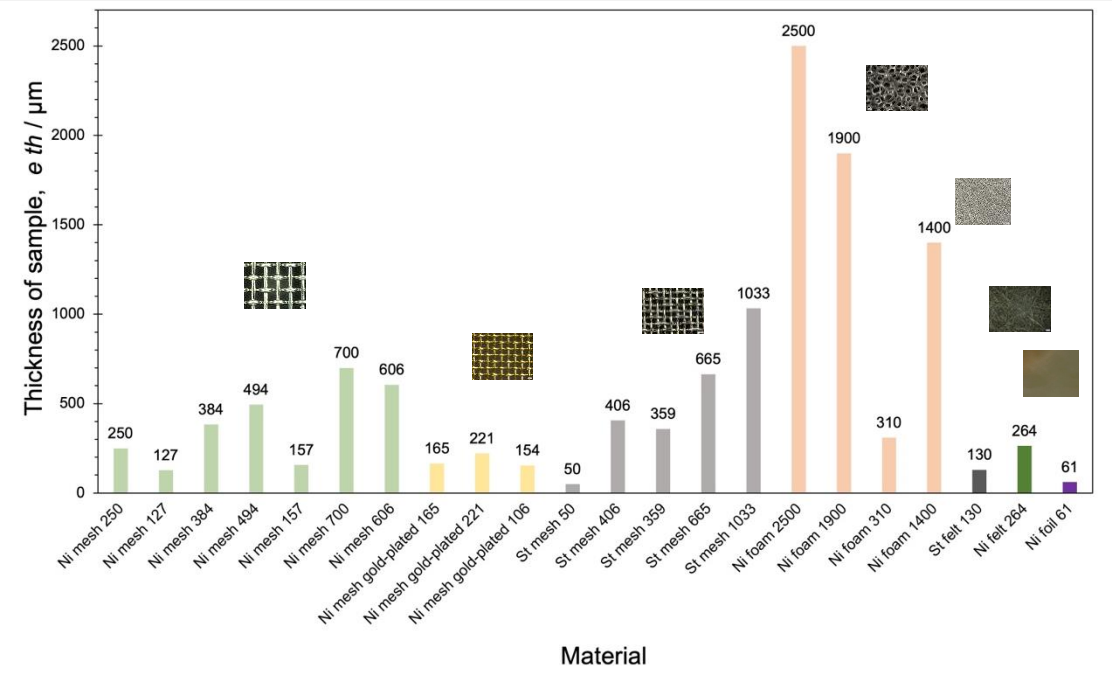

Figure 4: Thicknesses of industrially available materials

4.1.2. PORE/MESH SIZE

Pore/mesh size was measured using a mercury intrusion porosimeter Thermo Scientific Pascal 140/440 series (Thermo Fisher Scientific Inc., USA) (see Fig. 5) and a high-resolution digital microscope (see Fig. 1).

Figure 5: Mercury porosimeter Thermo Scientific Pascal 140/440 series (Thermo Fisher Scientific Inc., USA)

Pore/mesh size (width) of materials varies from 25 µm to 2500, in particular, the smallest Ni meshes width is 80 µm and the biggest – 1120 µm; gold-plated mesh width is in the rage of 106 to 500 µm, steel meshes – from 25 to 2500, foams – from 100 to 580 µm, steel felt – 130 µm, Ni felt – 50 µm (see Fig. 6, Tab. 2).

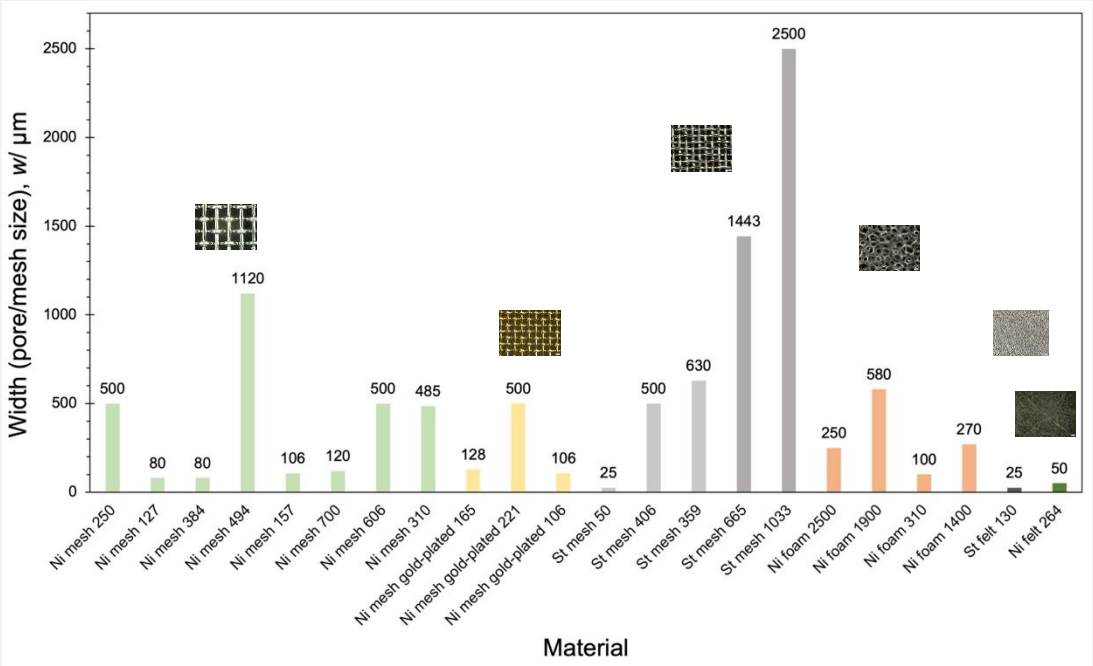

Figure 6: Pore/mesh size (width) of industrially available materials

4.2. PHYSICAL PROPERTIES

4.2.1. PERMEABILITY

Permeability was examined using the Porometer 3G series (Quantachrome Instruments, USA) (see Fig. 7). The rest was conducted in “dry” run mode with compressed air connected. Samples of the materials with a diameter of 16 mm were used. Fig. 8 illustrates a schematic view of the equipment commonly used for permeability evaluation (air-flow test) [12]. Evaluation of the data was carried out with the software 3GWin Version 2 (see Fig. 8). Permeability quantification is evaluated using the parameters derived from experimental data, such as fluid pressure and volumetric flow rate and the statistical method of linear regression (straight line fitting approach) was employed (see Fig. 9).

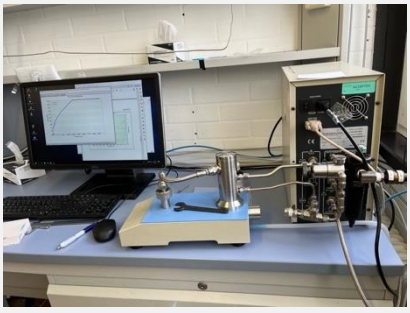

Figure 7: Porometer 3G series (Quantachrome Instruments, USA)

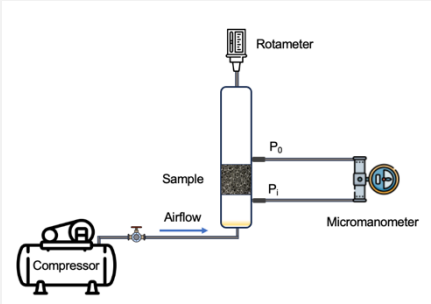

Figure 8: Schematics of equipment commonly used for permeability evaluation (air-flow test)

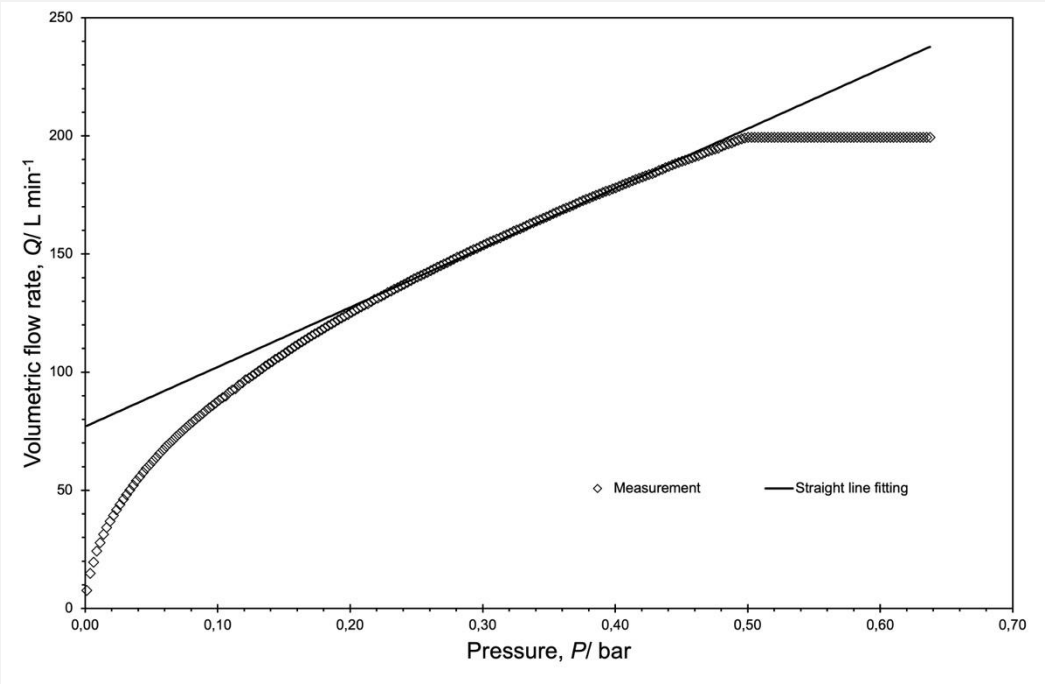

Figure 9: Typical dependence of volumetric flow rate and pressure through the porous/netted/felt medium of available materials

The calculated permeability is shown in Tab. 2 and Fig. 10. It is important to note that permeability data is closely correlated with pore/mesh size, meaning that permeability will decrease with a decrease in pore/mesh size.

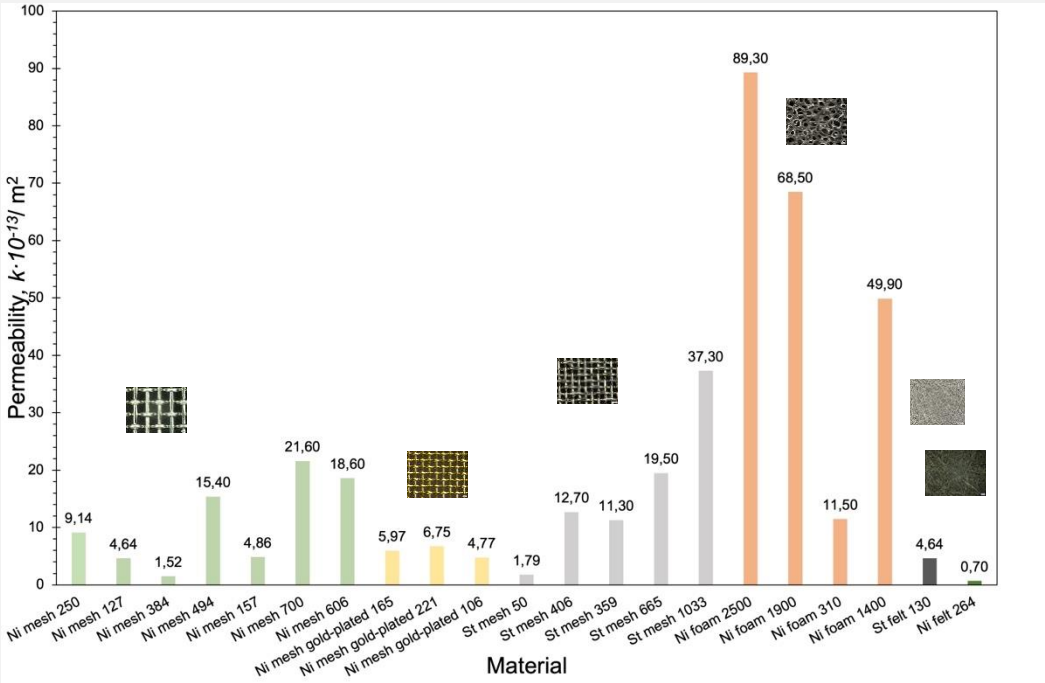

Figure 10: Permeability of industrially available materials

4.2.3. DENSITY AND POROSITY MEASUREMENT

The density and porosity of the samples were determined by helium pycnometer Picnomatic (Porotec GmbH, Germany) (see Fig. 11). Evaluation is based on the gas displacement approach.

4.2.3.1. DENSITY

Density values show minor deviations from the available theoretical data (see Tab. 2, Fig. 12).

Figure 11: Helium pycnometer Picnomatic (Porotec GmbH, Germany)

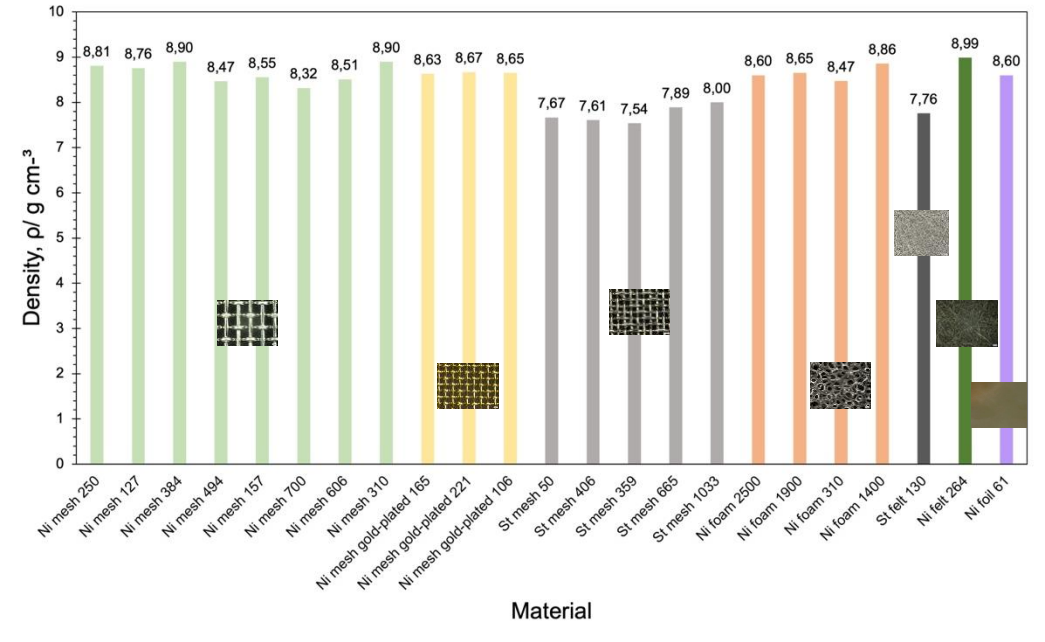

Figure 12: Density of industrially available materials

4.2.3.2. POROSITY MEASUREMENT

All materials, except plates, are highly porous (see Tab. 2, Fig. 13). Evaluated volumetric porosity was compared with theoretical values, which were calculated based on a theoretical and measured mass of samples. Evaluated results align with theoretical values.

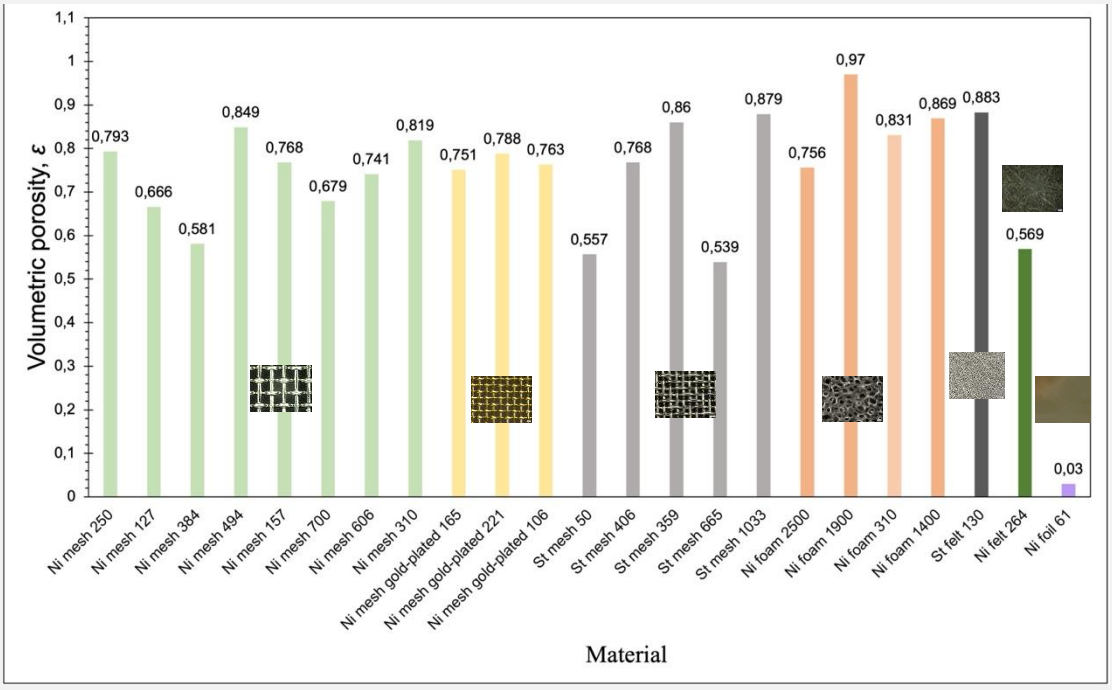

Figure 13: Porosity of industrially available materials

4.2.4. ELECTRICAL CHARACTERISTICS

The LORESTA-GX MSP resistivity measuring systems T610 (Mitsubishi Chemical Analytech Co., Japan) (see Fig. 14) were used along with the 4-pin sample method to evaluate the electrical conductivity, surface resistivity, and specific electrical resistance (ρ_v) measurements. Based on the results from Tab. 2, it is clear that Ni-based materials have lower specific electrical resistance than Fe-based materials.

Figure 14: Resistivity measuring systems LORESTA-GX MSP T610 (Mitsubishi Chemical Analytech Co., Japan)

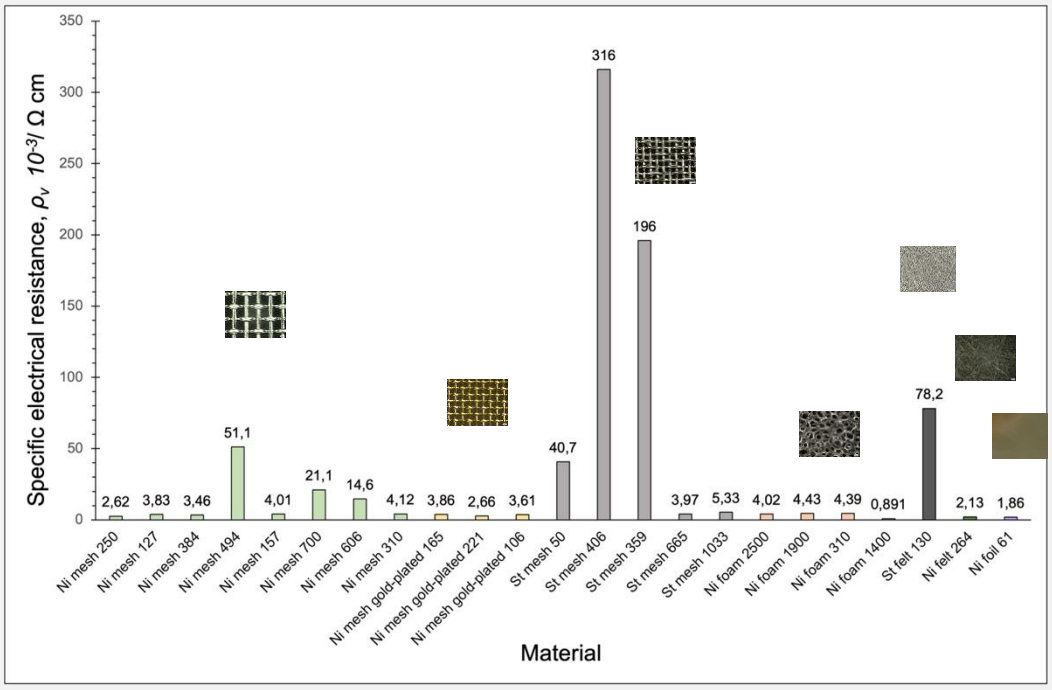

Figure 15: Specific electrical resistance of industrially available materials

5. ELECTROCHEMICAL PERFORMANCE

The samples were first washed with distilled water and sonicated in acetone solution for 3 min. The electrochemical characterizations were performed according to the test protocol (see Tab. 3) using the Gamry Reference 3000 potentiostat (Gamry Instruments, Warminster, PA, USA) in a three-electrode cell (see Fig. 16). The cell was constructed with steel mesh, steel felt, Ni foam, Ni mesh and Ni felt (d=3 cm^2) as the working electrode and counter electrode (made of the same material), and a reversible hydrogen electrode (RHE).

Figure 16: Flow-Through Setup for electrochemical characterization created in TU Claustahl

Polarization curves of the electrodes were obtained by linear sweep voltammetry (LSV) in a potential window of 1 to 1.8 V vs. RHE with a scan rate of 5 mV s^{-1}. Initially, the open circuit potentials (OCP) were settled for 25 min and then the polarization curves were recorded in 32 wt.% KOH aqueous solution (Windaus-Labortechnik GmbH & Co. KG) by 60°C.

Table 3: Electrochemical test protocol

	Test	**Conditions**
1.	Open Circuit Potential	25 min exposure;
2.	Cyclic Voltammetry	10 cycles; 0.0V to 0.6V vs. RHE (OER); 0.0V -0.6V vs. RHE (HER), scan rate 25 mV s^{-1};
3.	Linear sweep voltammetry	1 V to 1.8 V vs. RHE (OER); 0.0V to -0.6 V vs. RHE (HER), scan rate of 5 mV s^{-1};

Table 3: (continued)

4.	a) Chronopotentiometry b) Electrochemical impedance spectroscopy	i = 25, 50, 100, 200, 500 mA cm^{-2}; i = 25, 50, 100, 200, 500 mA cm^{-2}; frequency: 100 kHz – 0.1 Hz;
5.	Chronopotentiometry at various flow velocity	i= 200 mA cm^{-2}; v_s =1, 3, 5, 10 mm s^{-1};
	Time of measurements: 3-3.5 h	

The LSV results show that Fe-based materials are undoubtedly more electrochemically active than Ni-based materials for OER.

Electrochemical data (see Tab. 4, Fig. 17a) indicate better performance of OER on complex-structured electrodes like steel felts (sample 7, E_{OER}= 1.492V and 1.499V at current density 0.4 and 0.6A cm^{-2}, respectively). Presumably, this is due to the higher thickness of the sample and thus a higher active surface area. However, steel mesh with the smallest mesh size of 50 µm (sample 10, E_{OER} = 1.509V and 1.517V at current density 0.4 and 0.6 A cm^{-2}, respectively) demonstrates sufficient performance.

It is determined that Ni-based materials demonstrate a higher HER potential (-0.278V and -0.287V at current density 0.4 and 0.6A cm^{-2}, respectively) compared to Fe-based materials (-0.475V and -0.469V at current density 0.4 and 0.6A cm^{-2}, respectively) (see Tab. 4, Fig. 17b).

Ni mesh (-0.278 and -0.2871V at current density -0.4 and -0.6A cm^{-2}, respectively) and felt (-0.341V and -0.346V at current density -0.4 and -0.6 A cm^{-2}, respectively) exhibit higher activity for HER than foams (-0.370V and -0.383V at current density -0.4 and -0.6A cm^{-2}, respectively).

Table 4: Priority list of materials with respect to E_{HER} and E_{OER} compared at various current densities: -0.4; -0.6 (HER) and 0.4; 0.6 A/cm^2 (OER); Fe-based materials are highlighted with a grey background colour.

Sample	E_{HER} (V) at 0.4A cm^{-2}	Sample	E_{HER} (V) at -0.6A cm^{-2}	Sample	E_{OER} (V) at 0.4A cm^{-2}	Sample	E_{OER} (V) at 0.6A cm^{-2}
9	-0.278	9	-0.287	7	1.492	7	1.499
15	-0.339	15	-0.337	10	1.509	10	1.517
20	-0.341	19	-0.346	12	1.511	12	1.522
19	-0.354	20	-0.358	21	1.54	21	1.551
4	-0.367	4	-0.375	13	1.544	13	1.555
23	-0.370	18	-0.379	9	1.558	9	1.574
3	-0.370	6	-0.383	20	1.569	20	1.588
6	-0.370	3	-0.383	2	1.589	2	1.613
5	-0.378	5	-0.385	18	1.603	18	1.639
18	-0.380	23	-0.385	8	1.604	8	1.641
8	-0.401	8	-0.416	17	1.623	19	1.671
17	-0.410	17	-0.422	19	1.625	17	1.678
11	-0.421	11	-0.436	3	1.654	3	1.695
12	-0.475	12	-0.469	15	1.658	5	1.735
7	-0.476	21	-0.475	5	1.679	6	1.743
21	-0.479	7	-0.483	23	1.698	15	1.754
10	-0.488	10	-0.486	6	1.699	23	1.786
13	-0.492	13	-0.487	16	1.726	4	>1.800
16	-0.508	16	-0.519	11	1.757	11	>1.800
14	-0.525	14	-0.537	4	>1.800	16	>1.800
22	<-0.600	22	<-0.600	14	>1.800	22	>1.800
2	-	2	-	22	>1.800	14	>1.800

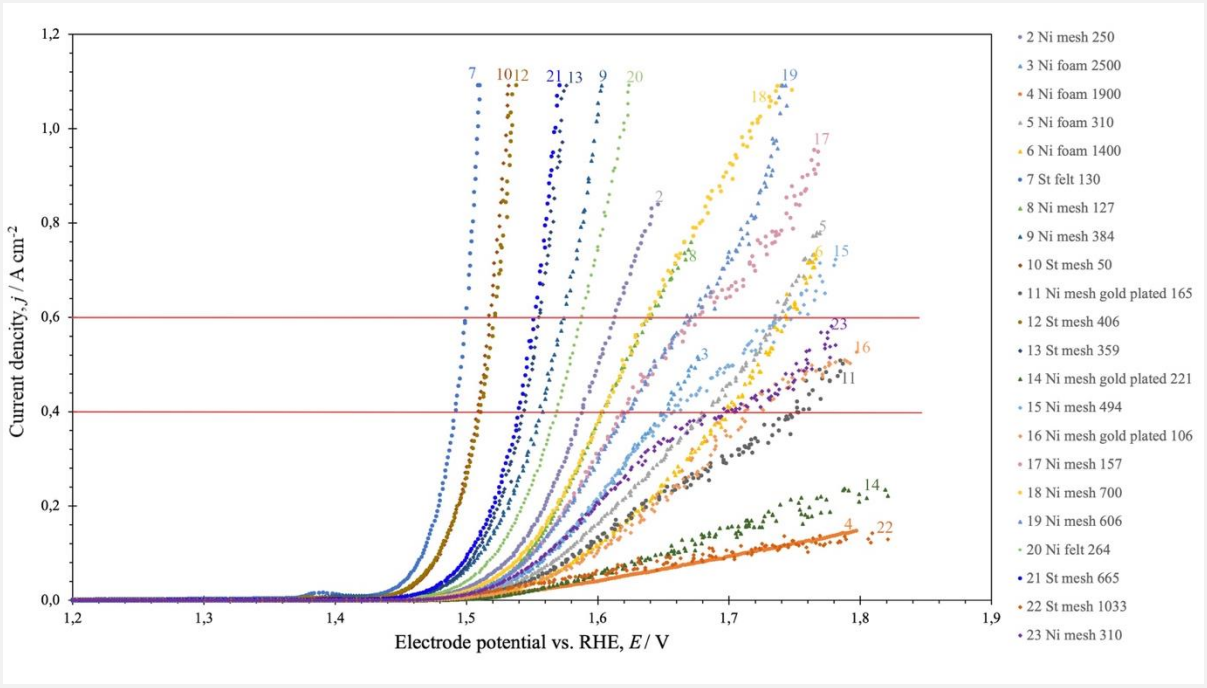

(a)

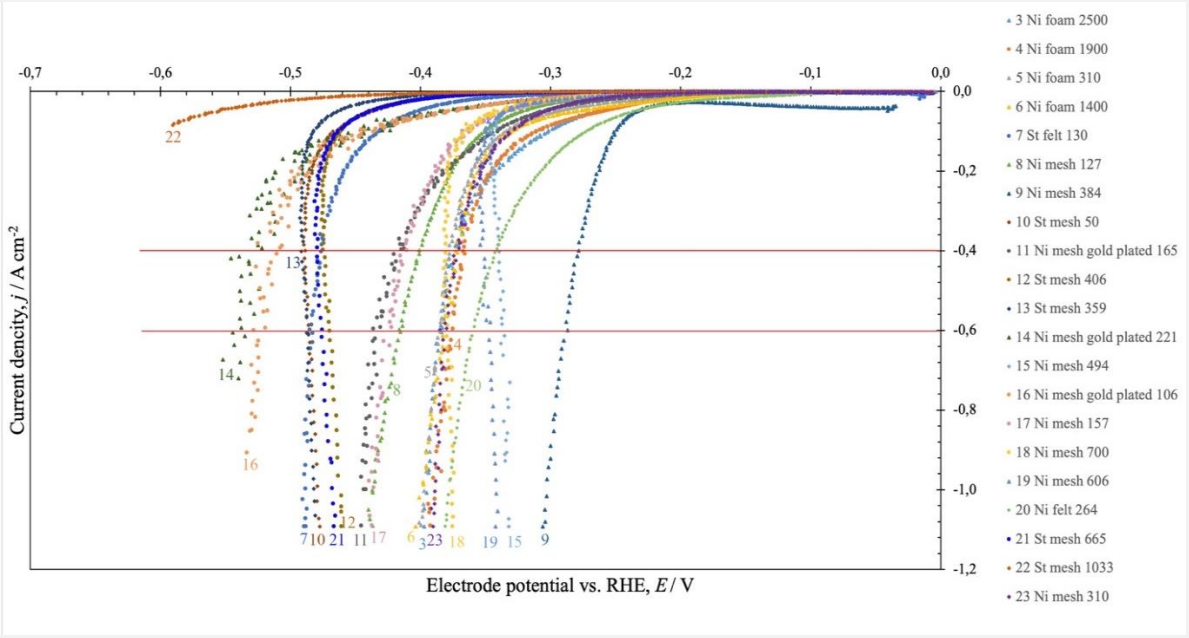

(b)

Figure 17: LSV curves (Tafel plots) using calculated real current density value for OER (a) and HER (b) performance of commercially available Ni-, Fe- based materials. Comparison of LCV polarization curves obtained at 5 mVs^{-1} scan rate in N_2-saturated 32% wt. KOH solution at 60 °C

Based on the results obtained at 3, 5 and 10 mm s^{-1} flow velocity presented in Tab. 5 and Fig. 18, higher flow velocity generally leads to a more stable and mainly lower overpotential. Data obtained at 1 mm s^{-1} flow velocity cannot be taken into account due to high standard deviation.

Table 5: Electrode potentials vs. RHE of commercially available Ni-, Fe- based materials obtained by flow velocity, v_S (mm s^{-1}): 1, 3, 5, 10. Fe-based materials are highlighted with a grey background colour.

Sample	E (V) at flow velocity, v_S =1 mm s^{-1}	E(V) at flow velocity, v_S =3 mm s^{-1}	E (V) at flow velocity, v_S =5 mm s^{-1}	E (V) at flow velocity, v_S = 10 mm s^{-1}
2	1.985	-	1.983	1.94
3	1.68*	1.855	1.841	1.802
4	1.5*	1.912	1.913	1.801
5	1.738*	1.835*	1.842	1.757
6	1.565**	1.917	1.861	1.773
7	1.758*	1.78	1.742	1.727
8	1.713*	1.832	1.85	1.762
9	-**	-**	4.108 (1653) **	1.698
10	1.737*	1.85	1.81	1.778
11	1.555*	1.874	1.889	1.805
12	0.772	0.771	0.864	1.755
13	1.521	1.832	1.828	1.816
14	1.565	2.302	2.3	1.86
15	1.564	1.929	1.956	1.861
16	1.815*	1.915	1.936	1.821
17	1.586	1.847	1.849	1.785
18	1.71*	1.884	1.861	1.775
19	0.01**	1.56	1.739	1.719
20	1.723**	1.715*	1.83	1.76
21	1.486	1.712	1.704	1.705
22	1.608	2.48	2.434	2.357
23	1.545	1.847	1.9	1.816

* Pulsed or waved shape of polarization plot.
** Data are invalid due to insufficient flow pressure in the electrochemical cell, samples were partially covered with electrolyte.

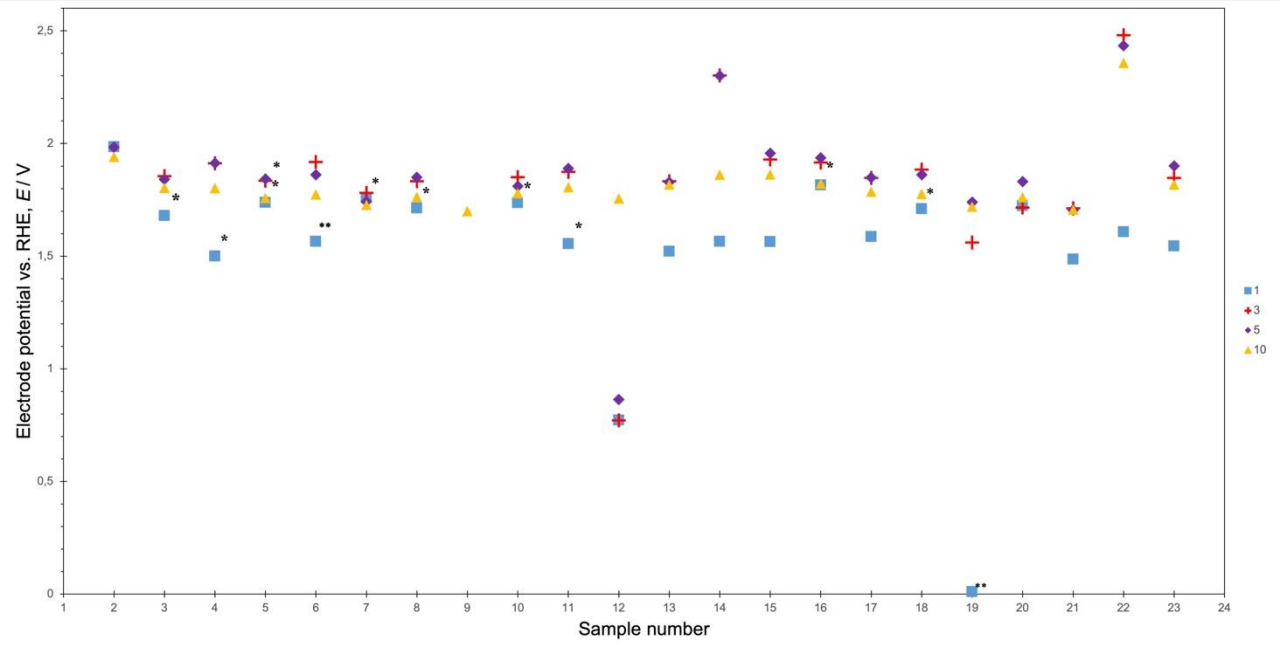

Figure 18: Electrode potentials of commercially available Ni-, Fe- based materials at various flow velocity, v_s (mm s^{-1}): 1, 3, 5 and 10 and current density, j = 200 mA cm^{-2}

6. CONCLUSION

1. All investigated materials meet basic requirements. However, Samples 11, 14, 16 (gold-plated Ni mesh) were investigated only as benchmark materials with a non-CRM substrate. These samples are excluded from the priority list due to gold being a CRM material and not meeting requirement 1.

2. It is evident that Ni-based materials exhibit better electrochemical performance for HER. Ni mesh (samples 9, 15, 19) and felt (20) demonstrate higher activity for HER than foams.

3. Fe-based materials are preferable to Ni-based materials for OER. Complex-structured steel felt (sample 7) and steel mesh (Samples 10, 12) show better electrochemical performance.

7. REFERENCES

[1] S. Cheng, B.E. Logan. Ammonia treatment of carbon cloth anodes to enhance power generation of microbial fuel cells // Electrochem. commun., V(9), 3(2007), pp. 492-496, ISSN 1388 2481, DOI: https://doi.org/10.1016/j.elecom.2006.10.023;

[2] J.M. Olivares-Ramírez, M.L. Campos-Cornelio, et al. Studies on the hydrogen evolution reaction on different stainless steels // Int. J. Hydrog., V(32), 15(2007), pp. 3170-3173, ISSN 0360 3199, DOI: https://doi.org/10.1016/j.ijhydene.2006.03.017;

[3] H. Hu, Y. Fan, et al. Hydrogen production in single-chamber tubular microbial electrolysis cells using non-precious-metal catalysts // Int. J. Hydrog., V(34), 20(2009), pp. 8535-8542, ISSN 0360-3199, DOI: https://doi.org/10.1016/j.ijhydene.2009.08.011;

[4] N.A. Salleh, S. Kheawhom, et al. Characterizations of nickel mesh and nickel foam current collectors for supercapacitor application // Arab. J. Chem., V(13), 8(2020), pp. 6838-6846, ISSN 1878-5352, DOI:https://doi.org/10.1016/j.arabjc.2020.06.036;

[5] H.I. Lee, H-S Cho, et al. The structural effect of electrode mesh on hydrogen evolution reaction performance for alkaline water electrolysis // Front. Chem., 787787, 9(2021), pp.1-10, DOI: https://doi.org/10.3389/fchem.2021.787787;

[6] G. Walther, B. Klöden, et al. A new class of high temperature and corrosion resistant nickel-based open-cell foams // Adv. Funct. Mater., V(10), 9(2008), 10.1002/adem.200800088, pp. 803-811, DOI: https://doi.org/10.1002/adem.200800088;

[7] H.Y. Cai, J.F. Ma, et al. Investigation on hydrogen evolution reaction performance of porous electrode prepared by laser powder bed fusion // Renew. Energ., V(185), 2022, pp. 771-778, ISSN 0960-1481, DOI: https://doi.org/10.1016/j.renene.2021.12.075;

[8] S.I. Torres, C.S. Elsheikh, et al. Porous Ni electrodes for hydrogen production from water electrolysis // Renew. Energy Power Qual. J., V(1), 11(2013), pp. 609-612, 10.24084/repqj11.385, DOI:10.24084/repqj11.385

[19] Y. Zhang, W. Cui, et al. Effect of the thickness of nickel electrode with aligned porous structure on hydrogen evolution reaction // Int. J. Hydrog., V(47), 28(2022), pp. 13552-13560, ISSN 0360-3199, DOI: https://doi.org/10.1016/j.ijhydene.2022.02.100;

[10] T. Zhang, Z. Ling. Template-assisted fabrication of Ni nanowire arrays for high efficient oxygen evolution reaction // Electrochim. Acta, V(318), 2019, pp. 91-99, ISSN 0013-4686, DOI: https://doi.org/10.1016/j.electacta.2019.06.063;

[11] R. Ding, S. Cui, et al. Improving the water splitting performance of nickel electrodes by optimizing pore structure using phase inversion method // Catal. Sci. Technol., 7, 2017, pp. 3056-3064, DOI:10.1039/C7CY00519A;
[12] M.D.M Innocentini, et al. Structure, manufacturing, properties and applications // M. Scheffler, P. Colombo (Eds.), Cel. Cer:, WILEY-VCH Verlag GmbH & Co. KGaA, Weinheim, 2009, pp. 313-341, ISBN: 3-527-31320-6.